Department of Complexity Science and Engineering
Graduate School of Frontier Sciences
The University of Tokyo

2022

Master's Thesis

Simulation Study of Continuum Damping for Alfvén Eigenmodes in Tokamak Plasmas

(トカマクプラズマにおけるアルヴェン固有モードに対する連続スペクトル減衰のシミュレーション研究)

Submitted September 1, 2022

Adviser: Professor Yasushi Todo

钟 新
Xin Zhong

Abstract

The frequency of Alfvén wave varies continuously with spatial location, forming a continuous frequency spectrum which is called Alfvén continuum. It is theoretically predicted that the continuous spectrum produces a phase mixing effect that strongly damps the Alfvén waves. This damping mechanism of Alfvén wave is called continuum damping. In tokamak plasmas, the coupling of poloidal harmonics m and $m + 1$ creates a frequency gap in the Alfvén continua, where toroidal Alfvén eigenmode (TAE) can exist without continuum damping. TAEs can be driven unstable by the resonant interaction with energetic particles whose orbit frequency is close to that of the TAE. TAEs can lead to the loss of energetic particles and deteriorate the plasma confinement. It is important to control the TAE instability.

In this thesis, we study the continuum damping with kinetic-magnetohydrodynamic hybrid simulations for a TAE with toroidal mode number $n = 4$. The effects of damping location, plasma density gradient, and bulk plasma pressure on continuum damping are investigated. The continuum damping is enhanced with closer damping location to the TAE. When the density decreases gradually with increasing radius, it reduces the difference in frequency of gaps. Steep density gradient enhances the continuum damping since it can enlarge the difference in frequency between the neighbouring gaps. Continuum damping for different values of uniform bulk plasma pressure is investigated. Continuum damping for the uniform pressure is stronger than that for the decreasing pressure profile.

It is demonstrated by the simulations that the continuum damping is stronger for the larger spatial gradient of the Alfvén continuum frequency, and the continuum damping rate converges to a constant level for weak dissipation. These results may contribute to the control of the TAEs in tokamaks.

Acknowledgement

First of all, I would like to express my sincere gratitude to my supervisor, Professor Yasushi TODO, who has provided me with various support during my graduate studies. His professional advice, careful explanation and patient guidance were invaluable for me. The MEGA code he developed also helped me understand the physics of plasma. The research was not able to be completed without my supervisor.

I would also like to thank everyone in MEGA group at National Institute for Fusion Science, Dr. Hao WANG, Dr. Malik IDOUAKASS, Dr. Jialei WANG, Dr. Panith Adulsiriswad, Hanzheng LI and Noriaki SUZUKI. Their positive attitude towards the research on nuclear fusion inspired me a lot. They have also offered me a great deal of help in my graduate studies.

Finally, I wish to thank my supportive parents. Their continuous encouragement assists me in overcoming barriers to my graduate studies.

Contents

Chapter 1

Introduction

1.1 Nuclear fusion

Since the beginning of the industrial revolution in the 1760s, production activities have shifted from handicraft to industrial production. The replacement of human labour by machines has led to a great increase in productivity. It is due to the rational use of energy by humans. The industrial revolution is also a revolution in energy conversion. However, with the upgrading of industrialisation, people began to exploit and utilise fossil energy endlessly.

Due to the non-renewable nature of fossil energy and the impact of global warming caused by greenhouse gas emissions from the use of fossil energy, the unsustainable use of fossil energy has led mankind to seek the use of renewable energy sources.

The enormous amount of energy continuously emitted by the sun has attracted scientists' attention. Nuclear fusion reactions are occurring continuously in the sun.

Nuclear fusion is the process by which two lighter mass nuclei combine to form a heavier nucleus and a lighter particle. The mass loss produced in this process releases enormous amounts of energy. The relationship between mass

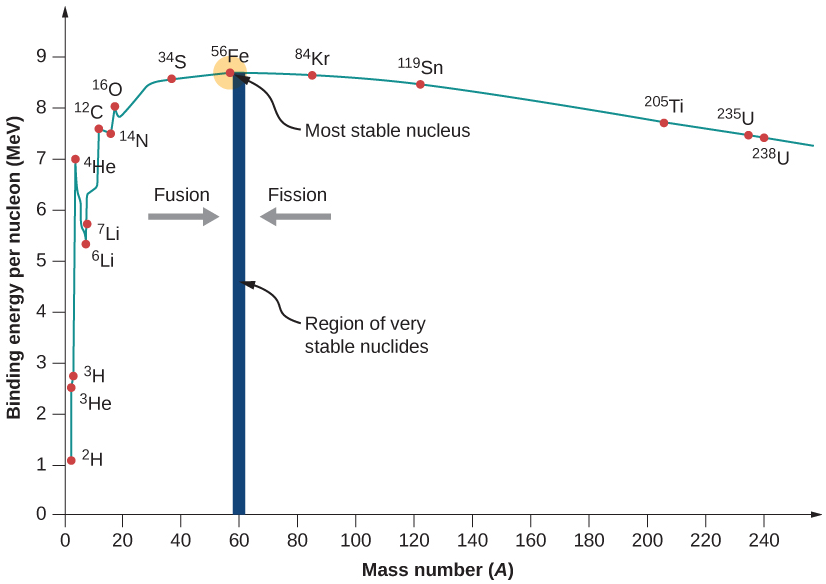

Figure 1.1: Nuclear binding energy per nucleon for different atomic number[1].

and energy conversion is pointed out by Einstein's mass-energy equivalence $E = mc^2$.

The ratio of the binding energy of an atomic nucleus to the number of protons and neutrons in the nucleus is called the specific binding energy. Starting from the hydrogen, the specific binding energy increases with the increase of the atomic number. The specific binding energy of iron is the highest and then begins to decrease slowly with increasing mass number. Energy is released when a nucleus with a lower specific binding energy is transformed into a nucleus with a higher specific binding energy. Thus, when a heavy nucleus undergoes a nuclear fission reaction or a light nucleus undergoes a nuclear fusion reaction, a large amount of energy is released.

Nuclear fission technology is currently being successfully used in nuclear power plants. Uranium is used as fuel to generate a large amount of thermal energy by fission. At present, the power generated by using nuclear fission in nuclear power plants have already accounted for 10% of global power generation.

However, nuclear fission reactions produce large amounts of radioactive waste that, if leaked into the environment, would cause an intractable disaster. In fact, this has happened many times in history.

Therefore, nuclear fusion, with its lower radioactive products, has a greater potential than fission for electricity generation.

1.2 Plasma and instability

It is necessary for the nucleus to get enough kinetic energy which could overcome the repulsive forces to reach the condition of fusion reaction. It means that the fuel of nuclear fusion have to be at very high pressure and temperature. As the temperature of substance increases, the binding between the nucleus and the electron in the atom will be broken, and the substance will consist of ions and free electrons. The quasi-neutral ionized gas, consisting of a large number of charged particles, is called plasma.

Plasma is usually classified into low temperature plasma and high temperature plasma. Low temperature plasma can be generated by gas discharge or high temperature combustion. The ionization level of low temperature plasma is not very high. Low temperature plasma has been widely used in various production fields. For example, it is now often used in semiconductor manufacturing equipment to etch silicon wafers.

In the nuclear fusion reaction, the matter is at an extremely high temperature and completely ionized, which is knowns as high temperature plasma. There is a large amount of high-temperature plasma in the universe. We need to confine the high-density and high-temperature plasma for a long enough time so that the condition of fusion reaction is achieved. The temperature, density and confinement time of the plasma need to satisfy Lawson's criterion.[2] For deuterium-tritium

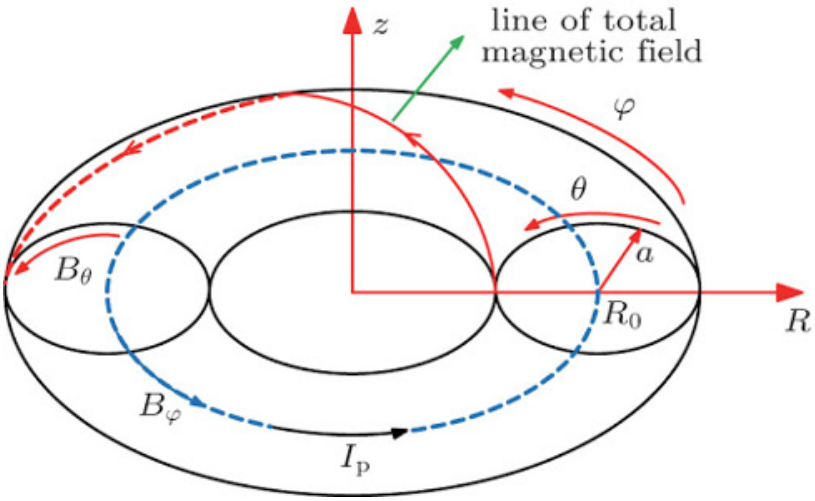

Figure 1.2: Schematic diagram of tokamak coordinate system.[3]

reaction, the product of density and confinement time should satisfy

$$n\tau > 10^{14} cm^{-3} s \, . \tag{1.1}$$

The minimum of $n\tau$ occurs near the temperature 26keV.

It is a very difficult problem to confine such a high-temperature and high-density plasma. To satisfy the condition, scientists are working on so-called magnetic confinement fusion, which uses the magnetic field. Magnetic confinement fusion uses a strong magnetic field to confine the plasma in a vacuum container, and uses a suitable method to heat the plasma to achieve sufficiently high temperature for nuclear fusion reaction.

Tokamak is one of the most popular magnetic confinement fusion devices and also considered to be the most feasible. Tokamak is a toroidal vacuum chamber. Strong magnetic field is generated by using toroidal and poloidal coils in order to confine the high temperature plasma.

In tokamak, the safety factor q is introduced to describe the twist of the mag-

netic field. The equation is defined by:

$$q = \frac{1}{2\pi} \int_0^{2\pi} \frac{d\phi}{d\theta} d\theta \tag{1.2}$$

where $d\phi$ and $d\theta$ are the poloidal angle and toroidal angle along the magnetic field line.

Different heating methods are used to heat the plasma in the tokamak to achieve sufficiently high temperature, which results in the background plasma with a large number of energetic particles. The interaction of these energetic particles with the background plasma will cause many instabilities, for example, the Alfvén wave instability.

1.3 Ideal magnetohydrodynamics (MHD)

Alfvén wave is a kind of low-frequency electromagnetic wave in plasma. The study of Alfvén waves is of great significance for controlled fusion. For example, it is practical to use Alfvén waves to heat the plasma. In addition, the interaction of Alfvén waves with energetic particles may cause plasma instability and deteriorate the plasma confinement.

The physical mechanism of Alfvén waves can be explained by magnetohydrodynamics (MHD). In a plasma, a large number of particles interact with each other, and the individual characteristics of the particles can be ignored for the collective motion. Treating such a large number of particles as individuals would make research very difficult. Therefore, we ignore the details of individual particles and treat the collective motion of a large number of particles as a fluid.

When we simplify the plasma as a system of fluid, we only need to focus on the macroscopic variables of the plasma. Although we regard plasmas as fluids, plasmas are made of charged particles, the electromagnetic forces on fluids should be considered.

The model to describe the behavior of the plasma which combines electromagnetics and fluid mechanics, is so-called MHD. The equations consist of Maxwell's equations and the equations of fluid mechanics.[4]

The mass continuity equation:

$$\frac{\partial \rho}{\partial t} + \nabla \cdot (\rho \boldsymbol{v}) = 0 \tag{1.3}$$

The momentum equation:

$$\frac{\partial}{\partial t}(\rho \boldsymbol{v}) + \nabla \cdot (\rho \boldsymbol{v}\boldsymbol{v}) = \boldsymbol{j} \times \boldsymbol{B} - \nabla p \tag{1.4}$$

Faraday's law:

$$\frac{\partial \boldsymbol{B}}{\partial t} = -\nabla \times \boldsymbol{E} \tag{1.5}$$

The energy equation:

$$\frac{d(\frac{p}{\rho^{\gamma}})}{dt} = 0 \tag{1.6}$$

Ampére's Law:

$$\nabla \times \boldsymbol{B} = \mu_0 \boldsymbol{j} \tag{1.7}$$

Ohm's law:

$$\boldsymbol{E} + \boldsymbol{v} \times \boldsymbol{B} = 0 \tag{1.8}$$

Here, $\boldsymbol{v}$ is the bulk plasma velocity, ρ is the mass density, p is the plasma pressure, $\boldsymbol{B}$ and $\boldsymbol{E}$ are the magnetic and electric fields, $\gamma = 5/3$ is the ratio of specific heats, $\boldsymbol{j}$ is the current density.

Chapter 2

Alfvén wave theory

2.1 Alfvén wave

Alfvén waves were proposed by the Swedish physicist Hannes Alfvén while studying the electrodynamics of the universe.[5] It is a low frequency electromagnetic wave that propagates in the plasma in the direction of the magnetic field. It is a transverse wave with the direction of vibration perpendicular to the direction of propagation. Figure 2.1 illustrates the propagation and oscillation of Alfvén wave.

In a plasma with infinite conductivity, the magnetic field can be viewed as frozen in the plasma. When there is a local perturbation perpendicular to the

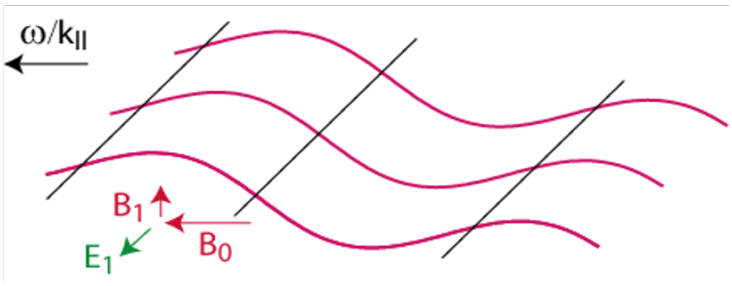

Figure 2.1: The propagation and oscillation of Alfvén wave[6]

direction of the magnetic field, the ionized material always tries to move with the magnetic lines of force in its motion perpendicular to the magnetic lines of force. In a way, the magnetic line of force moves together with the plasma motion, and the magnetic lines of force resist any perturbation with tensional restoring force, resulting in transverse oscillations, generating Alfvén waves.

The physical mechanism of an Alfvén wave is like a wave on a string under tension. The magnetic lines of force can be considered as strings whose mass density is equal to that of the plasma. There is a tension B^2/μ_0 on the magnetic line of force. Therefore, the propagation of oscillation on the magnetic line of force is very similar to the propagation of vibration on the string.

As the restoring force is provided by the magnetic tension, Alfvén wave frequency is related to the magnetic field and plasma density as well as the parallel wavenumber to the magnetic field. Alfvén velocity is represented by [7]

$$v_A = \frac{B}{\sqrt{\mu_0 \rho}} \tag{2.1}$$

where B, μ_0, ρ are magnetic field, vacuum magnetic permeability and bulk plasma density.

2.2 Alfvén continuum

In an inhomogeneous plasma, since the magnetic field and plasma density vary continuously with spatial location, the frequency of Alfvén wave also varies continuously with spatial location.

In tokamaks, the frequency of Alfvén waves is also related to the safety factor, which also varies continuously with spatial location, forming an Alfvén continuous spectrum which is called Alfvén contiuum. When the frequency of a wave is equal to the local Alfvén frequency, the wave resonates with the Alfvén continuum and is absorbed by the background plasma. This process can be utilized for plasma heating.

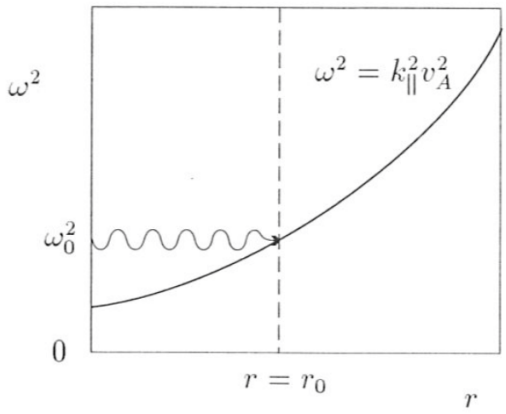

Figure 2.2: Cylindrical Alfvén continuum.[8]

2.3 Phase mixing

The continuous spectrum produces a phase mixing effect that strongly damps the Alfvén waves. The phase mixing effect of Alfvén waves can lead to resonant absorption.

The continuum corresponds to the superposition of many oscillations with different frequencies, oscillating with the local Alfvén frequency at various spatial locations. The perturbation with the uniform phase at the initial time oscillates with different frequency of continuous spectrum which varies depending on the position. In the time evolution, the oscillation phase differs for different positions. The difference in oscillation phase is larger for larger spatial gradient of the continuous spectrum $d\omega/dx$.[9]

The effects of many oscillations with different phases extinguish each other, resulting in reduced amplitude. Phase mixing results in continuum damping of Alfvén waves, which is hard for energetic particles to drive unstable. The damping rate is predicted to be proportional to the spatial gradient of the continuum frequency.[10] This is illustrated in Fig. 2.3.

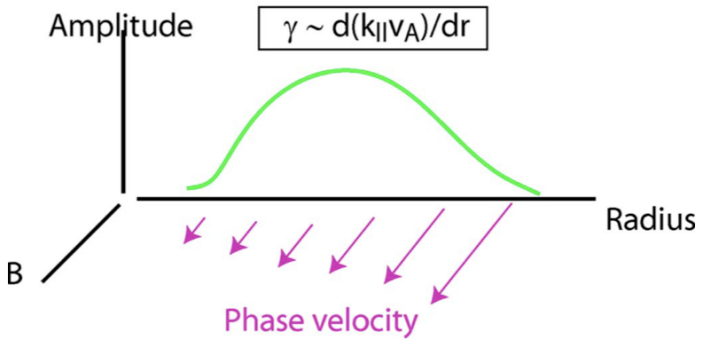

Figure 2.3: Damping rate γ is proportional to the spatial gradient of continuous spectrum frequency.[10]

2.4 Toroidal Alfvén eigenmode

In tokamaks, the toroidal effect produces gaps in the Alfvén continuous spectra, where the continuum damping of Alfvén waves disappears and thus Alfvén waves can be excited by energetic particles. In toroidal plasmas, the magnetic field strength varies in proportion to $1/R = 1/(R_0 + r\cos\theta)$ where R, R_0, r, and θ are major radius, major radius of the plasma center, minor radius, and poloidal angle, respectively (see Fig. 1.2). The $\cos\theta$ dependence of the magnetic field results in the coupling of neighbouring poloidal harmonics m and $m+1$ for Alfvén waves. The coupling of poloidal harmonics m and $m+1$ in toroidal plasmas creates a gap in the Alfvén continuous spectra, where toroidal Alfvén eigenmodes (TAEs) can exist. The wave numbers of the poloidal harmonics satisfy the condition:

$$k_m(r_0) = -k_{m+1}(r_0) \tag{2.2}$$

Since the frequency range of TAEs is close to the orbit frequency of energetic particles, TAE is a common unstable mode and easily excited by resonance so that the investigation of TAE is very important. In order to find a way to control the TAEs, it is necessary to understand the physical mechanism of the continuum damping of TAE.

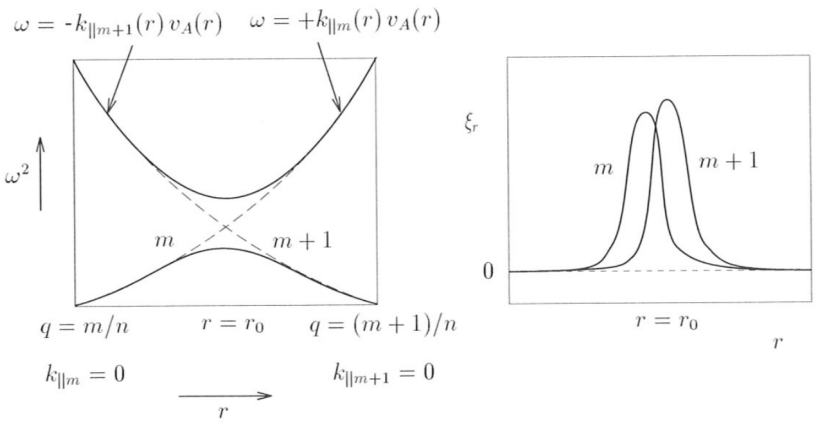

Figure 2.4: Coupling of poloidal harmonics m and $m+1$ in a toroidal plasma and toroidal Alfvén eigenmode (TAE) structure.[8]

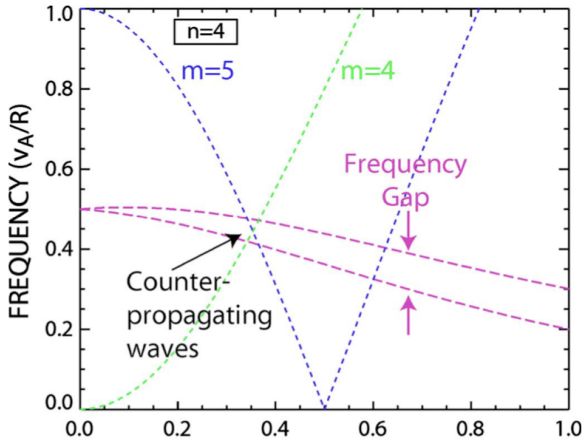

Figure 2.5: Dispersion relation of two waves with toroidal mode number $n = 4$ and poloidal mode numbers $m/m+1 = 4/5$. The two waves counter propagate each other and the coupling of two waves creates the frequency gap.[10]

2.5 Objective

The confinement of energetic particles is important to achieve the high temperature required for fusion reaction.

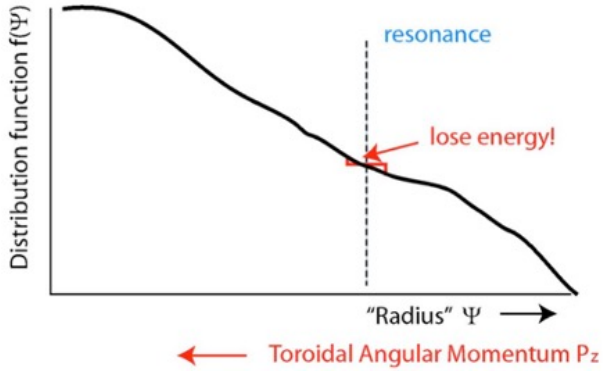

Figure 2.6: Energetic particle distribution function in tokamak[10]

In tokamak, toroidal canonical angular momentum is a constant of motion of charged particle and can be used as a radial coordinate for distribution function. The radial gradient of energetic-particle distribution function can destabilize Alfvén eigenmodes and Alfvén eigenmodes can transport energetic particles leading to energetic particle losses. Continuum damping is one of the stabilizing mechanisms of Alfvén eigenmodes. Therefore, the simulation study of continuum damping is important for the control of Alfvén eigenmodes and the energetic particle confinement.

Chapter 3

Simulation model

3.1 Equilibrium and instability

Various kinds of plasma instabilities can lead to the loss of energetic particles and the deterioration of the plasma confinement. Therefore, it is important to investigate the instabilities and understand the physical mechanisms of the instabilities.

It is necessary to know the stability of the equilibrium when we study the equilibrium configuration of the plasma. The stability of a system represents the evolution of the system when a perturbation is applied to the system. In general, if the equilibrium is unstable, a small perturbation grows exponentially and sometimes leads to the destruction of the equilibirum. The system is called stable if the perturbation does not grow and results in an oscillation.[11]

There is a huge amount of charged particles in the plasma, which means that it is a system with a very high degree of freedom. The evolution of such a system is very complex. The instability of plasma can be roughly divided into microscopic instability and macroscopic instability.[12]

The spatial nonuniformity of plasma distribution does not conform to Maxwell's distribution in velocity space. The non-Maxwellian distribution in velocity space may cause an instability, which is called microscopic instability. Microscopic in-

stability can be analyzed using kinetic theory, also known as kinetic instability. The instabilities caused by the inhomogeneity of the macroscopic variables such as pressure and magnetic field can modify the plasma shape. The physical mechanism of instability can be analyzed using the MHD theory.

Plasma can be considered as a continuous medium. Therefore, wave propagation in a plasma is a very important phenomenon. There are pressure, electric force, and magnetic force in the plasma, and these forces make various kinds of waves such as ion acoustic waves and Alfvén waves in the plasma.

3.2 MEGA code

MEGA code is a nonlinear hybrid simulation code which can compute the evolution of energetic particles interacting with an MHD fluid.[13] The nonlinear MHD equations are solved with dissipation terms. It provides a way to understand the behavior of energetic particles and MHD waves.

The nonlinear MHD equations interacting with the energetic particles are given below.[14]

$$\frac{\partial \rho}{\partial t} = -\nabla \cdot (\rho \boldsymbol{v}) + \nu_n \nabla^2 (\rho - \rho_{eq}) \tag{3.1}$$

$$\begin{aligned} \rho \frac{\partial \boldsymbol{v}}{\partial t} =& -\rho \boldsymbol{\omega} \times \boldsymbol{v} - \rho \nabla (\frac{v^2}{2}) - \nabla p + (\boldsymbol{j} - \boldsymbol{j}_h') \times \boldsymbol{B} \\ & - \nabla \times (\nu \rho \boldsymbol{\omega}) + \frac{4}{3} (\nu \rho \nabla \cdot \boldsymbol{v}) \end{aligned} \tag{3.2}$$

$$\frac{\partial \boldsymbol{B}}{\partial t} = -\nabla \times \boldsymbol{E} \tag{3.3}$$

$$\begin{aligned} \frac{\partial p}{\partial t} =& -\nabla \cdot (p \boldsymbol{v}) - (\gamma - 1) p \nabla \cdot \boldsymbol{v} \\ & + (\gamma - 1) \times \left[\nu \rho \omega^2 + \frac{4}{3} \nu \rho (\nabla \cdot \boldsymbol{v})^2 + \eta \boldsymbol{j} \cdot (\boldsymbol{j} - \boldsymbol{j}_{eq}) \right] \\ & + \nu_n \nabla^2 (p - p_{eq}) \end{aligned} \tag{3.4}$$

$$\boldsymbol{E} = -\boldsymbol{v} \times \boldsymbol{B} + \eta (\boldsymbol{j} - \boldsymbol{j}_{eq}) \tag{3.5}$$

$$\boldsymbol{\omega} = \nabla \times \boldsymbol{v} \tag{3.6}$$

$$\boldsymbol{j} = \frac{1}{\mu_0}\nabla \times \boldsymbol{B} \tag{3.7}$$

where ρ is bulk plasma density, $\boldsymbol{v}$ is velocity, ν_n is diffusion coefficient, $\boldsymbol{\omega}$ is vorticity, p is bulk plasma pressure, $\boldsymbol{j}$ is plasma current density, $\boldsymbol{j}'_h$ is energetic particle current density, $\boldsymbol{B}$ is magnetic field, $\boldsymbol{E}$ is electric field, ν is viscosity, η is resistivity, γ is adiabatic constant, and μ_0 is vacuum magnetic permeability. The subscript 'eq' represents equilibrium variables. The energetic-particle effect on the MHD fluid is taken into account by the term $\boldsymbol{j} - \boldsymbol{j}'_h$ in Eq. (3.2) where energetic-particle current density is subtracted from the total plasma current density.

The drift-kinetic model is employed for energetic particles. The guiding center velocity $\boldsymbol{u}$ is given below.[14]

$$\boldsymbol{u} = \boldsymbol{v}^*_{\parallel} + \boldsymbol{v}_{\boldsymbol{E}} + \boldsymbol{v}_{\boldsymbol{B}} \tag{3.8}$$

$$\boldsymbol{v}^*_{\parallel} = \frac{v_{\parallel}}{B^*}[\boldsymbol{B} + \rho_{\parallel} B\nabla \times \boldsymbol{b}] \tag{3.9}$$

$$\boldsymbol{v}_E = \frac{1}{B^*}[\boldsymbol{E} \times \boldsymbol{b}] \tag{3.10}$$

$$\boldsymbol{v}_B = \frac{1}{Z_h e B^*}[-\mu\nabla B \times \boldsymbol{b}] \tag{3.11}$$

$$\rho_{\parallel} = \frac{m_h v_{\parallel}}{Z_h e B} \tag{3.12}$$

$$\boldsymbol{b} = \boldsymbol{B}/B \tag{3.13}$$

$$B^* = B(1 + \rho_{\parallel}\boldsymbol{b} \cdot \nabla \times \boldsymbol{b}) \tag{3.14}$$

$$m_h v_{\parallel}\frac{dv_{\parallel}}{dt} = \boldsymbol{v}^*_{\parallel} \cdot [Z_h e\boldsymbol{E} - \mu\nabla B] \tag{3.15}$$

where $v_{\parallel}$ is the velocity parallel to the magnetic field, $\boldsymbol{v}_E$ is $\boldsymbol{E} \times \boldsymbol{B}$ drift velocity, $\boldsymbol{v}_B$ is $\nabla \boldsymbol{B}$ drift, μ is magnetic moment, m_h and $Z_h e$ are mass and electric charge of energetic particles.

The energetic particle current density $\boldsymbol{j}'_h$ is given by

$$\boldsymbol{j}'_h = \int (\boldsymbol{v}^*_{\parallel} + \boldsymbol{v}_B) Z_h e f d^3v - \nabla \times \int \mu \boldsymbol{b} f d^3v \tag{3.16}$$

where $\boldsymbol{E} \times \boldsymbol{B}$ drift velocity $\boldsymbol{v}_E$ disappears in $\boldsymbol{j}'_h$ due to the quasi-neutrality, and f is the distribution function.

Chapter 4

Simulation results of continuum damping

4.1 Toroidal Alfvén eigenmode without continuum damping

We start our study with a toroidal Alfvén eigenmomde (TAE) without continuum damping. We investigate a TAE with toroidal mode number $n = 4$. The spatial profiles of safety factor, density, and pressure for the initial equilibrium are shown in Fig. 4.1. While the safety factor increases with the radius, the density is uniform in the whole plasma. The Alfvén continua for toroidal mode number $n = 4$ are shown in Figure 4.2. We see that the frequency gap induced by the coupling between neighbouring poloidal mode numbers m and $m + 1$ is open throughout the plasma from the center to the edge.

A simulation of a TAE with $n = 4$ was performed for this initial equilibrium. The viscosity and the diffusion coefficient are chosen to be $\nu = \nu_n = 5 \times 10^{-7} v_A R_0$ and resistivity is chosen to be $\eta = 5 \times 10^{-7} \mu_0 v_A R_0$. Figure 4.3 shows the spatial profile of radial MHD velocity for the TAE. It can be seen clearly in Fig. 4.3 that

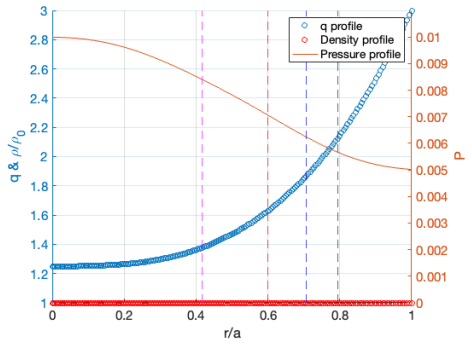

Figure 4.1: Spatial profiles of safety factor (q), density, and pressure for the initial equilibrium.

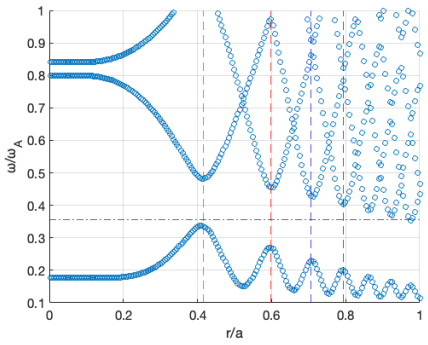

Figure 4.2: Alfvén continua for toroidal mode number $n = 4$ for the initial equilibrium shown in Fig. 4.1. Horizontal line represents the frequency of the TAE.

the dominant poloidal harmonics are $m/m+1 = 5/6$. The frequency of the TAE is shown by the horizontal line in Fig. 4.2. The frequency of the TAE does not intersect with the Alfvén continua.

The spatial profiles of the viscous and resistive dissipations are investigated for the TAE. The viscous and joule heating terms are respectively proportional to viscosity ν and resistivity η. The viscous dissipation is represented by $\nu\rho\omega^2 + \frac{4}{3}\nu\rho(\nabla \cdot \boldsymbol{v})^2$ and the resistive dissipation is represented by $\eta\boldsymbol{j} \cdot (\boldsymbol{j} - \boldsymbol{j}_{eq})$ in Eq. (3.4). The spatial profiles of viscous and resistive dissipations for the TAE are shown in Fig. 4.4. We see in the figure that the dissipations peak at the location where the radial MHD velocity profiles peak as shown in Fig. 4.3.

The time evolution of energy (ΔE_A), dissipation rate, driving rate, and growth rate is shown for the TAE in Fig. 4.5. The driving rate represents the rate of energetic-particle energy transfer to the TAE energy. The difference between the driving rate and the dissipation rate is the growth rate of the TAE energy. The energy dissipation rate of the TAE without continuum damping is 1.067% normalized by the Alfvén frequency $\omega_A = v_A/R_0$. The energy dissipation rate of

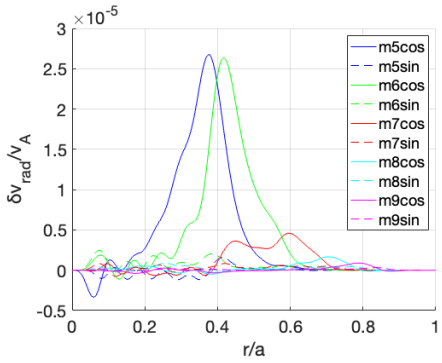

Figure 4.3: Spatial profiles of radial MHD velocity harmonics of the TAE.

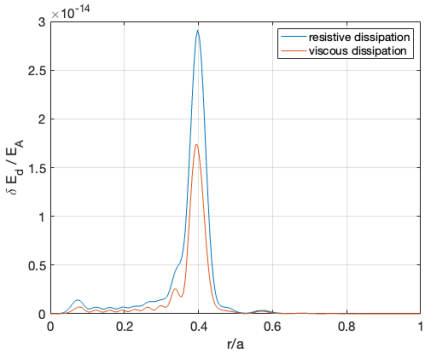

Figure 4.4: Spatial profiles of viscous and resistive dissipations for the TAE without continuum damping.

the TAE without continuum damping will be compared to that with continuum damping investigated in the following sections.

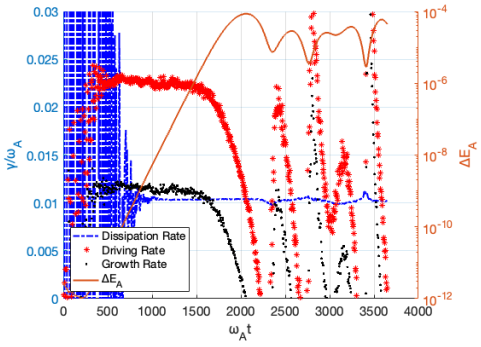

Figure 4.5: Time evolution of energy (ΔE_A), energy dissipation rate, driving rate, and growth rate for the TAE.

4.2 Effects of density profile on continuum damping

Continuum damping for the TAE with toroidal mode number $n = 4$ has been investigated for different density profiles. Since the local Alfvén velocity depends

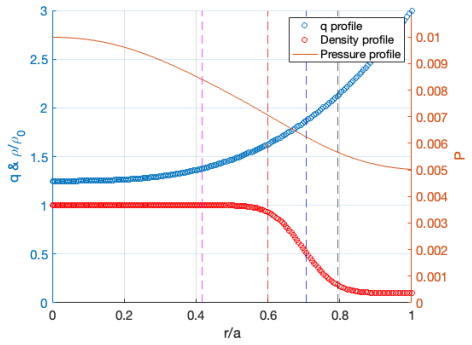

Figure 4.6: Spatial profiles of safety factor (q), density with r_{trans}=0.7 and $\Delta r = 0.1$, and pressure.

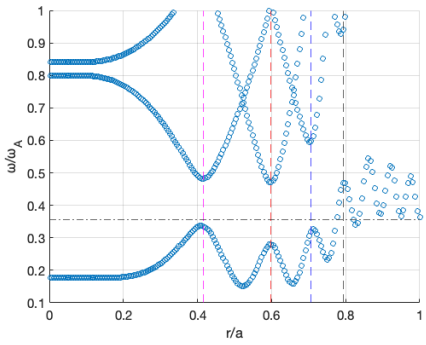

Figure 4.7: Alfvén continua for the density profile with r_{trans}=0.7 and $\Delta r = 0.1$.

on density, the Alfvén continuous spectra depend on the density profile. The density should decrease to raise the frequency of the Alfvén continua at the plasma edge so that continuum damping occurs. The normalized density profile at the normalized radius $x = r/a$ is described by

$$\rho_{nor}(x) = 0.1 + 0.45(\frac{2}{\sqrt{\pi}} \int_{\frac{x-r_{trans}}{\Delta r}}^{\infty} e^{-t^2} dt) \tag{4.1}$$

where r_{trans} controls the position of density decrease and Δr controls the gradient of density decrease. The normalized density is $\rho_{nor}(0) = 1$ at the plasma center and $\rho_{nor}(1) = 0.1$ at the plasma edge.

As the dominant poloidal harmonics of the TAE without continuum damping are $m/m+1 = 5/6$, the continuum damping with poloidal harmonics $m = 6, 7$, and 8 is investigated for different density profiles.

4.2.1 Continuum damping for $r_{trans} = 0.7$

The continuum gap induced by the coupling of $m/m+1 = 8/9$ harmonics is located at $q = \frac{2m+1}{2n} = 2.125$, which corresponds to the normalized radius $r/a = 0.8$. For the investigation of continuum damping near this continuum gap, we

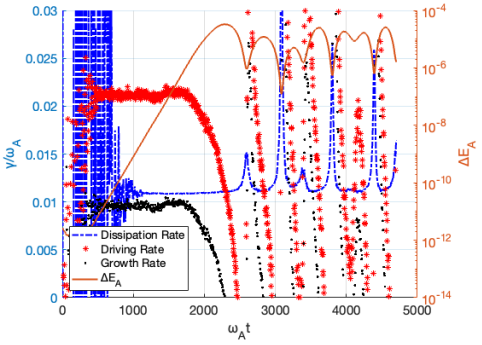

Figure 4.8: Time evolution of energy (ΔE_A), energy dissipation rate, driving rate, and growth rate for the TAE.

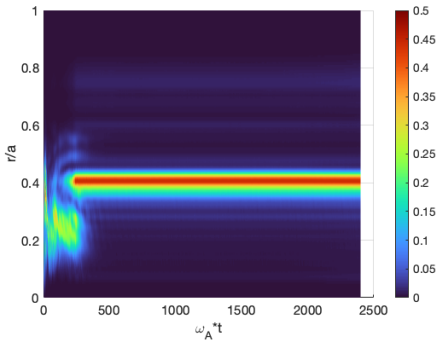

Figure 4.9: Time evolution of energy dissipation profile for the density profile with r_{trans}=0.7 and $\Delta r = 0.1$.

use a density profile with r_{trans}=0.7 and $\Delta r = 0.1$. The spatial profiles of safety factor, density, and pressure are shown in Fig. 4.6, and the Alfvén continua are shown in Fig. 4.7. We see in Fig. 4.7 that the frequency of the Alfvén continua rises beyond $r/a = 0.7$. The central frequency of the gap which is induced by the coupling of $m/m + 1 = 8/9$ is higher than the frequency of the TAE. Then, we can expect that continuum damping occurs around $r/a = 0.8$.

The time evolution of energy (ΔE_A), energy dissipation rate, driving rate, and growth rate is shown for the TAE in Fig. 4.8. The energy dissipation rate of the TAE normalized by the Alfvén frequency is 1.089% which is close to that for the uniform density 1.067%. The time evolution of energy dissipation profile is shown in Fig. 4.9. As is shown in the figure, the energy dissipation does not increase obviously comparing with the uniform density case. The spatial profile of energy dissipation is contributed by Joule heating and viscous heating. It provides the evidence for continuum damping since the phase mixing enhance the viscous and resistive dissipation. There is a very low energy dissipation around the normalized radius of 0.8, where continuum damping is expected to take place. It means that the continuum damping is very weak although it takes place.

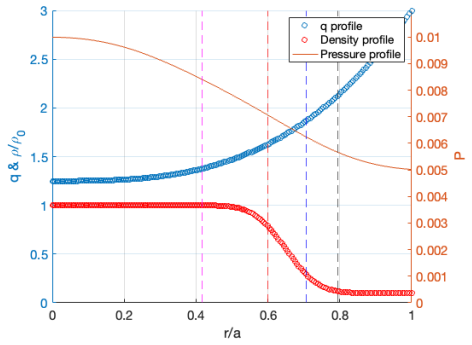

Figure 4.10: Spatial profiles of safety factor (q), density with r_{trans}=0.65 and $\Delta r = 0.1$, and pressure.

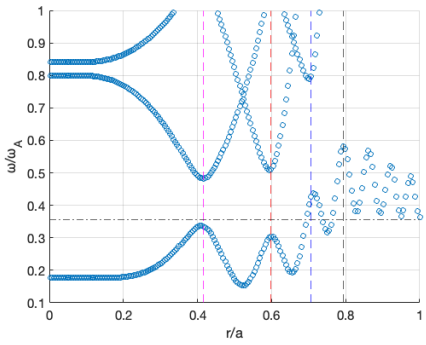

Figure 4.11: Alfvén continua for the density profile with $r_{trans} = 0.65$ and $\Delta r = 0.1$.

4.2.2 Continuum damping for $r_{trans} = 0.65$

The continuum gap induced by the coupling of $m/m+1 = 7/8$ harmonics is located at $q = \frac{2m+1}{2n} = 1.875$, which corresponds to the normalized radius $r/a = 0.7$. For the investigation of continuum damping near this continuum gap, we use a density profile with $r_{trans} = 0.65$ and $\Delta r = 0.1$. The spatial profiles of safety factor, density, and pressure are shown in Fig. 4.10, and the Alfvén continua are shown in Fig. 4.11. We see in Fig. 4.11 that the frequency of the Alfvén continua rises beyond $r/a = 0.65$. We expect that continuum damping occurs around $r/a = 0.7$.

The time evolution of energy (ΔE_A), energy dissipation rate, driving rate, and growth rate is shown for the TAE in Fig. 4.12. The energy dissipation rate of the TAE normalized by the Alfvén frequency is 1.184% which is slightly higher than that for the uniform density 1.067%. The time evolution of energy dissipation profile is shown in Fig. 4.13. We see a substantial energy dissipation at the continuum damping around $r/a = 0.7$ in the linearly growing phase and the clear enhancement of energy dissipation in the nonlinear phase after the saturation of the instability.

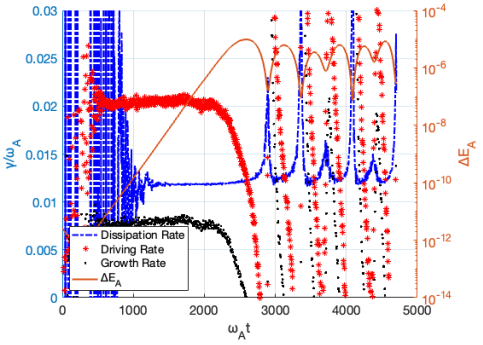

Figure 4.12: Time evolution of energy (ΔE_A), energy dissipation rate, driving rate, and growth rate for the TAE.

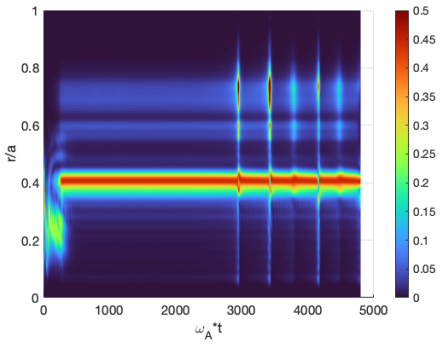

Figure 4.13: Time evolution of energy dissipation profile for the density profile with r_{trans}=0.65 and $\Delta r = 0.1$.

4.2.3 Continuum damping for $r_{trans} = 0.5$

The continuum gap induced by the coupling of $m/m+1 = 6/7$ harmonics is located at $q = \frac{2m+1}{2n} = 1.625$, which corresponds to the normalized radius $r/a = 0.6$. For the investigation of continuum damping near this continuum gap, we use a density profile with $r_{trans} = 0.5$ and $\Delta r = 0.1$. The spatial profiles of safety factor, density, and pressure are shown in Fig. 4.14, and the Alfvén continua are shown in Fig. 4.15. We see in Fig. 4.15 that the frequency of the Alfvén continua rises beyond $r/a = 0.5$. We expect that continuum damping occurs around $r/a = 0.55$.

The time evolution of energy (ΔE_A), energy dissipation rate, driving rate, and growth rate is shown for the TAE in Fig. 4.16. The energy dissipation rate of the TAE normalized by the Alfvén frequency is 1.231% which is higher than that for the uniform density 1.067%. The time evolution of energy dissipation profile is shown in Fig. 4.17. We see a substantial energy dissipation at the continuum damping around $r/a = 0.55$ in the linearly growing phase and the clear enhancement of energy dissipation in the nonlinear phase after the saturation

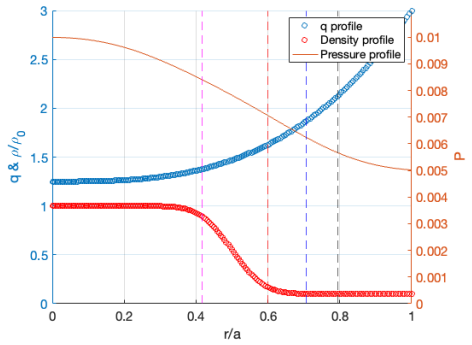

Figure 4.14: Spatial profiles of safety factor (q), density with r_{trans}=0.5 and $\Delta r = 0.1$, and pressure.

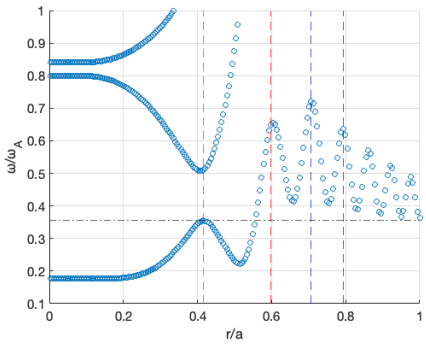

Figure 4.15: Alfvén continua for the density profile with $r_{trans} = 0.5$ and $\Delta r = 0.1$.

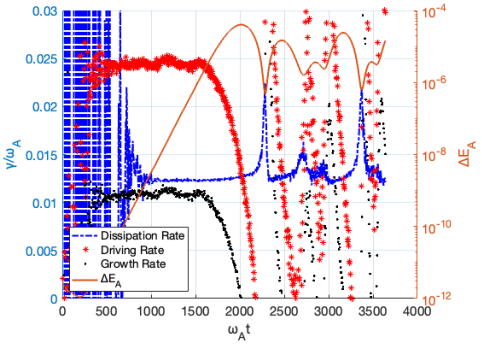

Figure 4.16: Time evolution of energy (ΔE_A), energy dissipation rate, driving rate, and growth rate for the TAE.

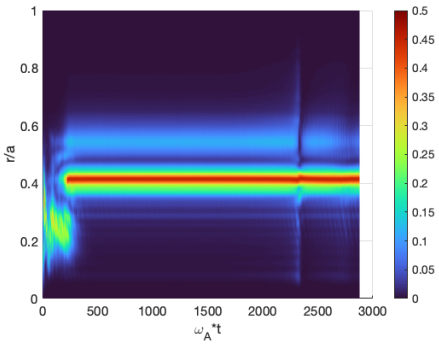

Figure 4.17: Time evolution of energy dissipation profile for the density profile with r_{trans}=0.5 and $\Delta r = 0.1$.

of the instability.

4.3 Effect of density gradient

In this section, we investigate the effect of density gradient on continuum damping. The density gradient is determined by the parameter Δr in the density profile given by Eq. (4.1). The parameter Δr is set to be 0.05 and 0.2 with the parameter $r_{trans} = 0.5$. The value of Δr=0.05 would provide the maximum density at the location of the first gap and the minimum density at the location of the second gap. This will lead to a strong continuum damping if the damping rate is related to density gradient. The density gradient is weak for $\Delta r = 0.2$. All the cases investigated in this section share the same safety factor and pressure profiles in order to find the relationship between damping rate and density gradient.

The spatial profiles of safety factor, density, and pressure are shown in Figs. 4.18 and 4.19. The Alfvén continua are shown in Figs. 4.20 and 4.21. We see in the figures that the frequency of the gap induced by the coupling of poloidal harmonics $m/m+1 = 6/7$ with the steep density gradient is higher than that with the weak density gradient. It should be noticed that the normalized frequency of TAE increases to $0.405\omega_A$ for $\Delta r = 0.2$ since the normalized density at the location of TAE decreases.

The time evolution of energy (ΔE_A), energy dissipation rate, driving rate, and growth rate is shown for the TAE in Figs. 4.22 and 4.23. We see in Fig. 4.22 an outstanding increase in energy dissipation rate for the steep density gradient profile, and a slight decrease in energy dissipation rate for the weak density gradient in Fig. 4.23. The energy dissipation rate of the TAE normalized by the Alfvén frequency for the steep density gradient shown in Fig. 4.22 is 1.531% which is substantially higher than that for the uniform density 1.067%. The energy dissipation rate for the weak density gradient shown in Fig. 4.23 is 1.189%. These

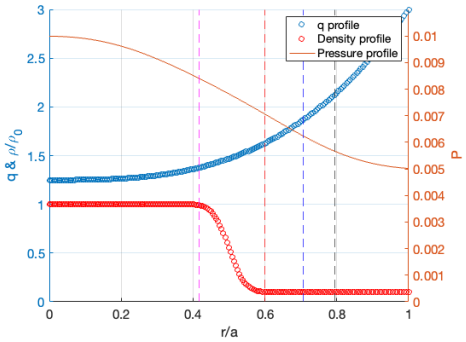

Figure 4.18: Spatial profiles of safety factor (q), density with r_{trans}=0.5 and $\Delta r = 0.05$, and pressure.

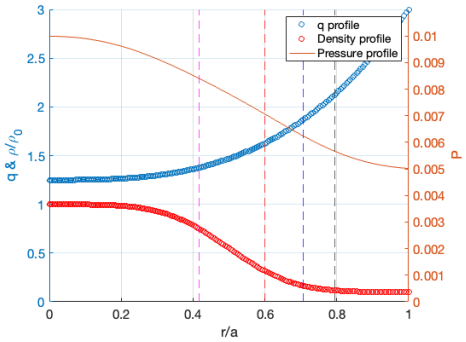

Figure 4.19: Spatial profiles of safety factor (q), density with r_{trans}=0.5 and $\Delta r = 0.2$, and pressure.

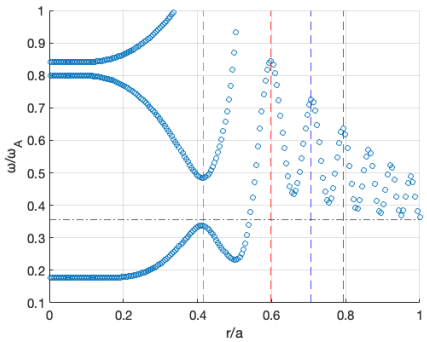

Figure 4.20: Alfvén continua for the density profile with r_{trans}=0.5 and $\Delta r = 0.05$.

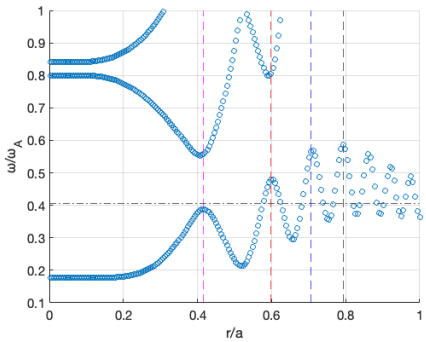

Figure 4.21: Alfvén continua for the density profile with r_{trans}=0.5 and $\Delta r = 0.2$.

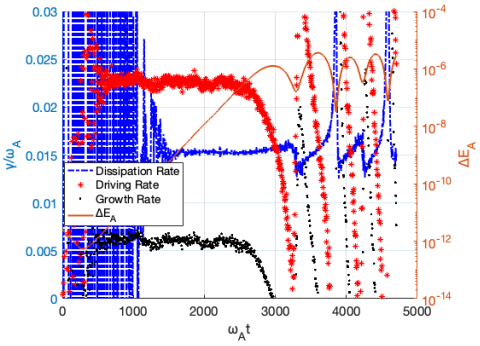

Figure 4.22: Time evolution of energy (ΔE_A), energy dissipation rate, driving rate, and growth rate for the TAE for r_{trans}=0.5 and $\Delta r = 0.05$.

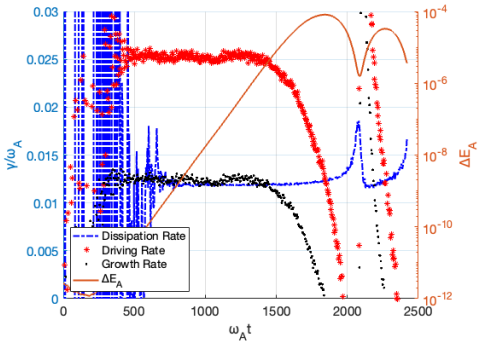

Figure 4.23: Time evolution of energy (ΔE_A), energy dissipation rate, driving rate, and growth rate for the TAE for r_{trans}=0.5 and $\Delta r = 0.2$.

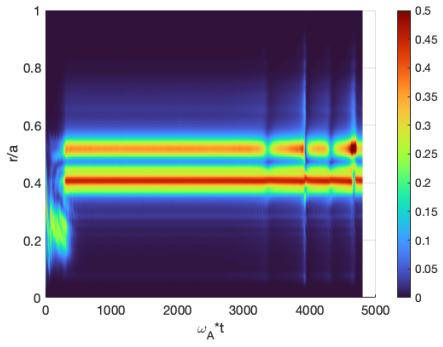

Figure 4.24: Time evolution of energy dissipation profile for the density profile with r_{trans}=0.5 and $\Delta r = 0.05$.

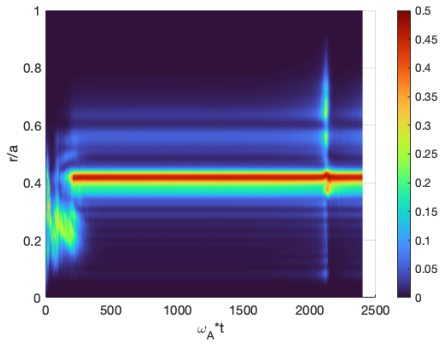

Figure 4.25: Time evolution of energy dissipation profile for the density profile with r_{trans}=0.5 and $\Delta r = 0.2$.

results prove that density gradient affects significantly the strength of continuum damping.

The time evolution of energy dissipation profile is shown in Figs. 4.24 and 4.25. We see in Fig. 4.24 that the energy dissipation for the steep density gradient is extremely high at the location of continuum damping. The energy dissipation for the weak density gradient shown in Fig. 4.25 is reduced to a low level, which is similar to the cases with larger r_{trans} where continuum damping occurs far away from the TAE.

4.4 Effect of uniform pressure

All the simulations we discussed above were performed for a pressure profile decreasing with radius. Such a pressure profile reduces the spatial variation of Alfén continua for the decreasing density profile with increasing radius. In this section, we investigate different cases with uniform pressure profile of different pressure levels. The density profile is given by $r_{trans} = 0.5$ and $\Delta r = 0.05$. Low pressure values 0.25% and 0.5% normalized by B_0^2/μ_0 where B_0 is the magnetic field at the plasma center are assumed. The spatial profiles of safety factor, density, and pressure are shown in Figs. 4.26 and 4.27. The Alfvén continua are shown in Figs. 4.28 and 4.29.

The time evolution of energy (ΔE_A), energy dissipation rate, driving rate, and growth rate is shown for the TAE in Figs. 4.30 and 4.31. The energy dissipation rate of the TAE normalized by the Alfvén frequency is 1.692% and 1.742 % for uniform pressure 0.25% and 0.5%, respectively. Both the low constant pressure levels strengthen the continuum damping effect comparing to the simulation with gradually decreasing pressure profile. The higher constant pressure results in a higher damping rate, which suggests that large difference in frequency between neighbouring gaps enhance the continuum damping.

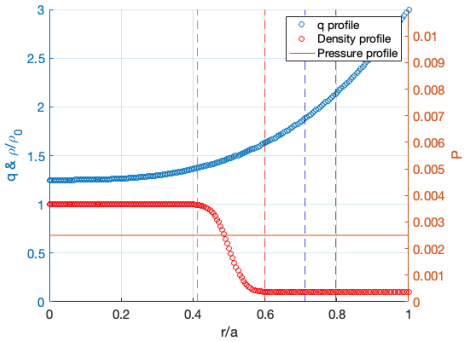

Figure 4.26: Spatial profiles of safety factor (q), density, and pressure. The pressure profile is uniform $p = 2.5 \times 10^{-3} B_0^2/\mu_0$.

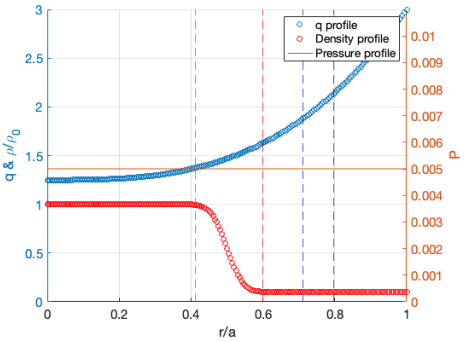

Figure 4.27: Spatial profiles of safety factor (q), density, and pressure. The pressure profile is uniform $p = 5.0 \times 10^{-3} B_0^2/\mu_0$.

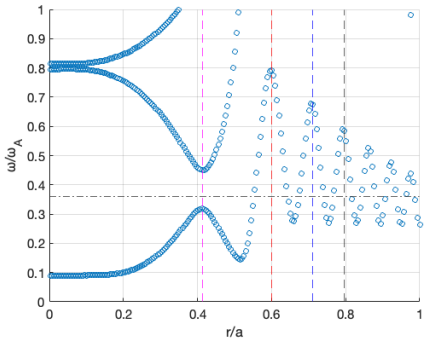

Figure 4.28: Alfvén continua with uniform pressure $p = 2.5 \times 10^{-3} B_0^2/\mu_0$.

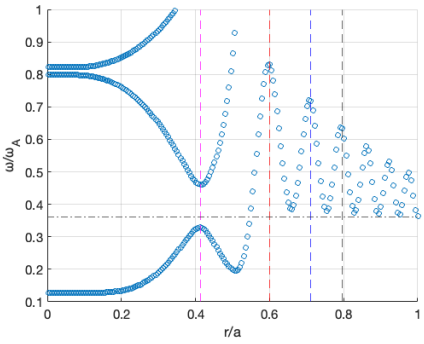

Figure 4.29: Alfvén continua with uniform pressure $p = 5.0 \times 10^{-3} B_0^2/\mu_0$.

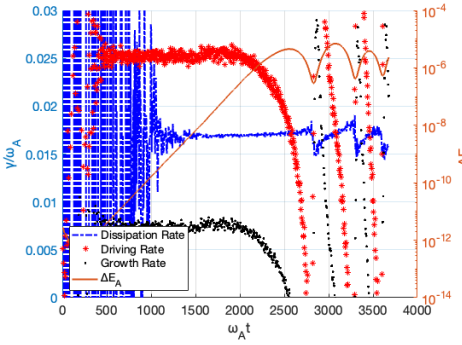

Figure 4.30: Time evolution of energy (ΔE_A), energy dissipation rate, driving rate, and growth rate for the TAE for uniform pressure $p = 2.5 \times 10^{-3} B_0^2/\mu_0$.

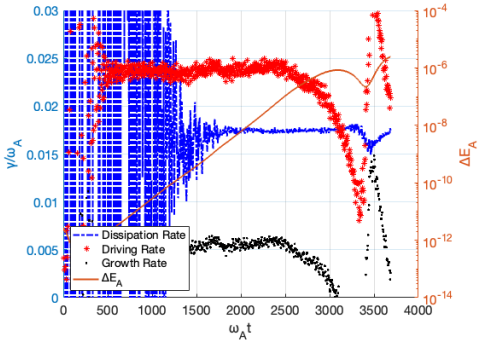

Figure 4.31: Time evolution of energy (ΔE_A), energy dissipation rate, driving rate, and growth rate for the TAE for uniform pressure $p = 5.0 \times 10^{-3} B_0^2/\mu_0$.

Another equilibrium with uniform pressure of 1% was also investigated. The spatial profiles of safety factor, density, and pressure are shown in Fig. 4.32, and the Alfvén continua are shown in Fig. 4.33. The frequency of the gap induced by the coupling of $m/m+1 = 6/7$ harmonics reaches $0.9\omega_A$. The time evolution of energy (ΔE_A), energy dissipation rate, driving rate, and growth rate is shown for the TAE in Fig. 4.34. The energy dissipation rate does not reach a constant level with large fluctuations. On the other hand, the driving rate hovers around a level close to the other simulations while the growth rate is almost 0. The TAE energy does not grow exponentially. The values of driving rate and growth rate give an evidence that the dissipation rate is comparable to the driving rate. The time evolution of energy dissipation profile is shown in Fig. 4.35. The energy dissipation at the location of the continuum damping ($r/a \sim 0.55$) is higher than that at the spatial peak location of the TAE ($r/a \sim 0.4$). The saturation amplitude of radial MHD velocity is low around $v_r/v_A \sim 10^{-9}$ which is extremely small comparing to 10^{-5} for the TAE without continuum damping. The spatial profile of radial MHD velocity of the TAE is shown in Fig. 4.36.

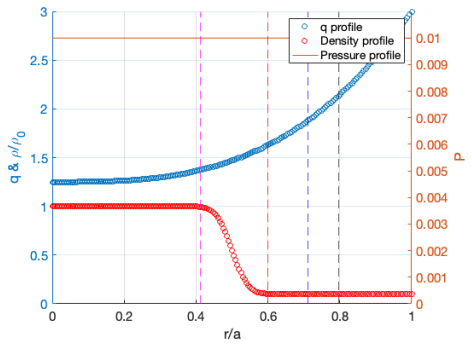

Figure 4.32: Spatial profiles of safety factor (q), density, and pressure. The pressure profile is uniform $p = 1.0 \times 10^{-2} B_0^2/\mu_0$.

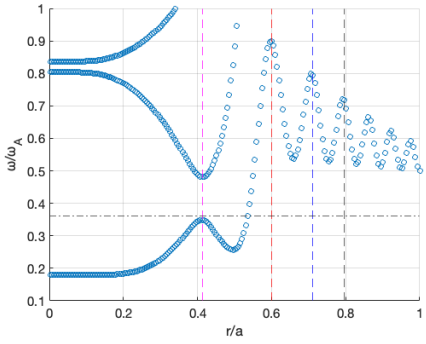

Figure 4.33: Alfvén continua with uniform pressure $p = 1.0 \times 10^{-2} B_0^2/\mu_0$.

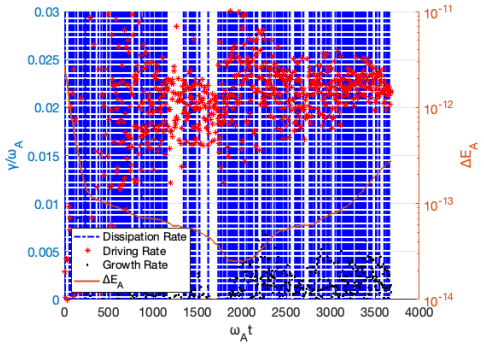

Figure 4.34: Time evolution of energy (ΔE_A), energy dissipation rate, driving rate, and growth rate for the TAE for uniform pressure $p = 1.0 \times 10^{-2} B_0^2/\mu_0$.

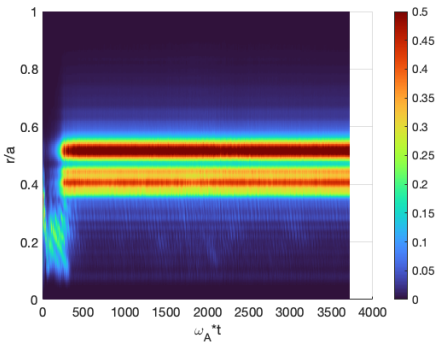

Figure 4.35: Time evolution of energy dissipation profile for uniform pressure $p = 1.0 \times 10^{-2} B_0^2/\mu_0$.

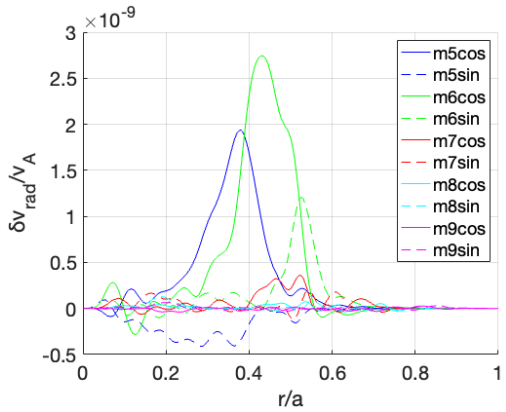

Figure 4.36: Spatial profile of radial MHD velocity of the TAE for uniform pressure $p = 1.0 \times 10^{-2} B_0^2/\mu_0$ with strong continuum damping.

4.5 Nonlinear evolution

The nonlinear evolution of continuum damping is also an interesting research topic. The energy dissipation rate varies in time for the strong continuum damping cases. For example, The dissipation rate increases significantly to a high level in Fig. 4.22, while the dissipation rate even decreases slightly in Fig. 4.30. The spatial profile of radial MHD velocity of the TAE in the nonlinear evolution with high energy dissipation rate shown in Fig. 4.22 is presented in Fig. 4.37. The spatial profile of radial MHD velocity of the TAE is shown in Fig. 4.38 for the linearly growing phase in the same simulation .

It can be clearly seen that the sine part of radial MHD velocity with high energy dissipation rate has a fluctuation comparing to the radial MHD velocity in the linearly growing phase. It might be pointed out that the strong phase mixing which results in the high energy dissipation rate causes the fluctuation in the sine part of radial MHD velocity.

The evolution of energy dissipation rate also has a relationship with the evolution of mode frequency. The frequency evolution is shown in Figs. 4.39 and

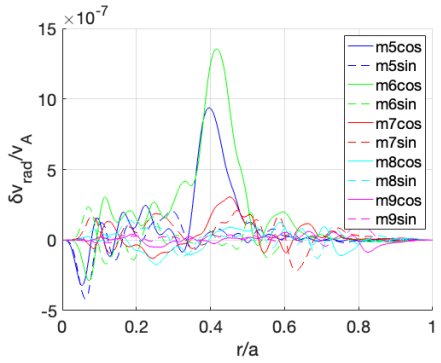

Figure 4.37: Spatial profile of radial MHD velocity of the TAE in the nonlinear evolution with high energy dissipation rate.

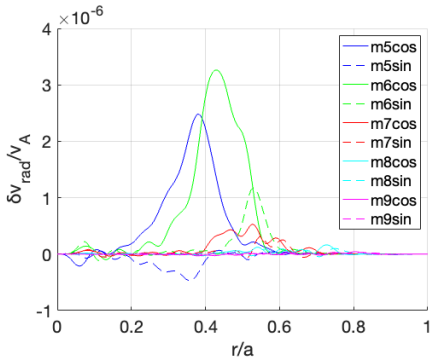

Figure 4.38: Spatial profile of radial MHD velocity of the TAE in the linearly growing phase.

4.40 for the cases shown in Figs. 4.22 and 4.30, respectively. The frequency has a similar trend to the energy dissipation rate in the nonlinear evolution. It is possible that the mode frequency is affected by the strong phase mixing in the nonlinear evolution.

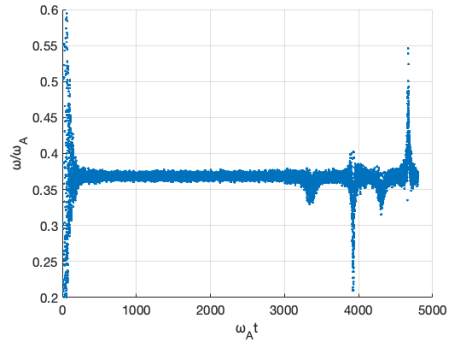

Figure 4.39: Time evolution of the TAE frequency for the case shown in Fig. 4.22.

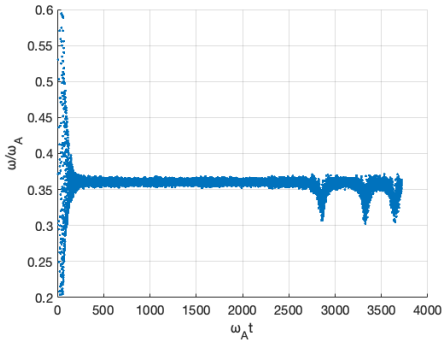

Figure 4.40: Time evolution of the TAE frequency for the case shown in Fig. 4.30.

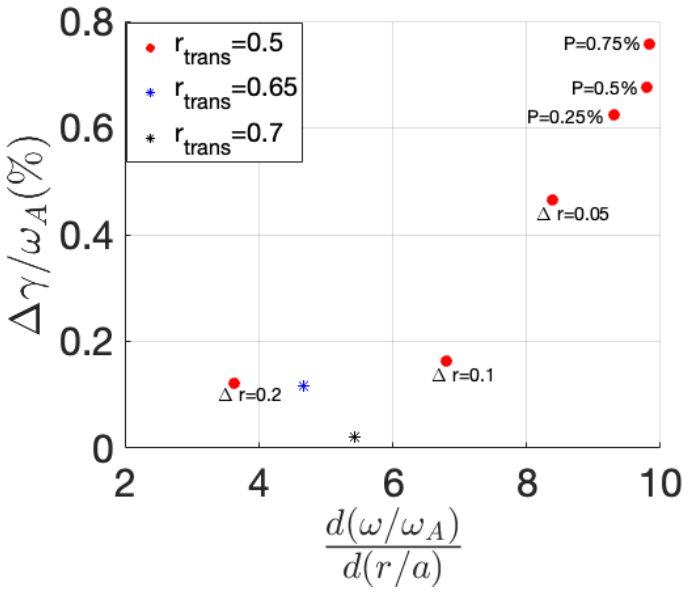

Figure 4.41: Continuum damping rate versus radial gradient of Alfvén continuum frequency.

4.6 Dependence of continuum damping on the radial gradient of Alfvén continuum frequency

We plot in Fig. 4.41 the continuum damping rate versus the radial gradient of Alfvén continuum frequency for the simulations we performed. The continuum damping rate is defined by the increase in energy dissipation rate from that for the basic case without continuum damping. As it is hard to measure the energy dissipation rate for the uniform pressure of 1%, it is replaced by a case with uniform pressure 0.75%, where the energy dissipation rate is 1.823%. We can confirm the strong dependence of the continuum damping on the radial gradient of Alfvén continuum frequency for the same r_{trans}. The blue and black points represent the cases with $r_{trans} = 0.65$ and 0.7. The continuum damping is weak for the cases with $r_{trans} = 0.65$ and 0.7 where the damping location is far away from TAE.

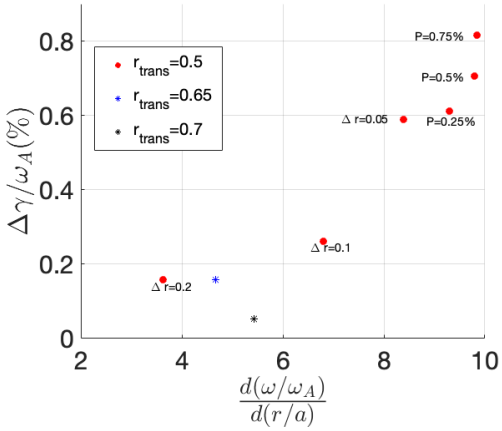

Figure 4.42: Continuum damping rate versus radial gradient of Alfvén continuum frequency for $\nu = \nu_n = 10^{-7} v_A R_0$ and $\eta = 10^{-7} \mu_0 v_A R_0$

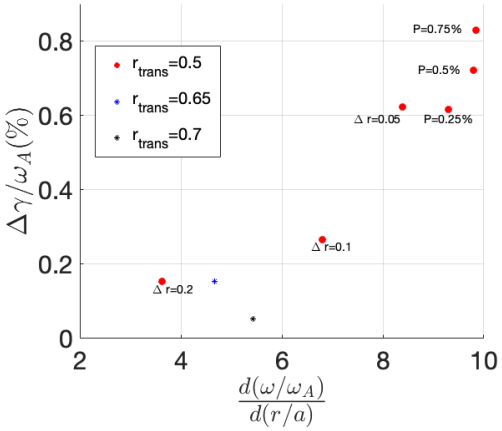

Figure 4.43: Continuum damping rate versus radial gradient of Alfvén continuum frequency for $\nu = \nu_n = 5 \times 10^{-8} v_A R_0$ and $\eta = 5 \times 10^{-8} \mu_0 v_A R_0$

The continuum damping rate versus the radial gradient of Alfvén continuum frequency are shown for different diffusion coefficients in Figs 4.42 and 4.43. The basic damping rate of TAE without continuum damping for $\nu = \nu_n = 10^{-7} v_A R_0$ and $\eta = 10^{-7} \mu_0 v_A R_0$ is 0.304%. The basic damping rate of TAE without continuum damping for $\nu = \nu_n = 5 \times 10^{-8} v_A R_0$ and $\eta = 5 \times 10^{-8} \mu_0 v_A R_0$ is 0.203%. It is found that the continuum damping rate converges to a constant level for weak dissipation in each case while the basic damping rate is affected significantly by dissipation coefficients.

Chapter 5

Conclusion

Alfvén wave phase mixing theory was proposed to explain the coronal heating problem in solar physics.[9] It indicates that the difference in oscillation phase is larger for larger gradient of the continuous spectrum. The viscous and resistive dissipation are enhanced due to phase mixing. We have investigated numerically this damping mechanism of Alfvén wave, which is called continuum damping, for the toroidal Alfvén eigenmodes (TAEs) in the tokamak plasmas.

The local Alfvén continuum frequency in tokamak is given by

$$\omega_m = k_m v_A \approx \frac{nq - m}{qR} v_A \ . \tag{5.1}$$

For the cross position (r_0) of neighbouring poloidal harmonics m and $m+1$, the following relationship is satisfied:

$$\omega_m^2(r_0) = \omega_{m+1}^2(r_0) \ . \tag{5.2}$$

The central frequency of TAE gap is given by

$$\omega_{gap} \approx \frac{1}{2qR} v_A = \frac{B}{2qR\sqrt{\mu_0 \rho}} \tag{5.3}$$

where B, q, R, μ_0, ρ are magnetic field, safety factor, major radius, vacuum magnetic permeability and bulk plasma density.

In this thesis, we investigated numerically the continuum damping of TAEs with kinetic-MHD hybrid simulations. It was found that the continuum damping is enhanced with closer damping location to the TAE. The safety factor profile decides the location of gaps, while the density profile and the magnetic field decide the frequency of gaps. Steep density gradient at the damping location enlarge the difference in frequency between the neighbouring gaps. Continuum damping for the uniform pressure is stronger than that for the decreasing pressure profile.

Large difference in frequency between the neighbouring gaps provide greater spatial gradient of Alfvén continuum frequency at the damping location. The simulation results demonstrated that the continuum damping of TAE is stronger for larger spatial gradient of the Alfvén continuum frequency, and the continuum damping rate converges to a constant level for weak dissipation. The continuum damping does not depend on the dissipation coefficients when they are sufficiently weak.

These results may provide some ways to control Alfvén eigenmodes. For example, we can control plasma density by gas puffing and control magnetic field by current drive. With the control of the density profile and the magnetic field, one can enlarge the spatial gradient of the Alfvén continuum frequency at the position close to the Alfvén eigenmodes.

The physical mechanism of continuum damping is the enhancement of viscous and resistive dissipation.[15] Additionally, a research pointed out magnetosonic waves are nonlinearly generated by Alfvén wave phase mixing. The Alfvén wave heats the plasma indirectly due to the dissipation of magnetosonic waves.[16] The efficiency of the nonlinear generation of magnetosonic waves is determined by the frequency of the Alfvén waves, the gradient in the background Alfvén velocity, and the bulk plasma pressure.[17] This process may be related to the strong continuum damping with high bulk plasma pressure found in this

thesis. The nonlinear generation of magnetosonic waves by Alfvén wave phase mixing should be further researched in future.

Bibliography

[1] Samuel J. Ling. et al, University Physics Volume 3, OpenStax University Physics.

[2] Lawson, J. D., 1955, Proceedings of the Physical Society, Section B. 70 (1): 6–10.

[3] Xiong Hao, Liu Ming-Hai, Chen Ming, Rao Bo, Chen Jie, Chen Zhao-Quan, Xiao Jin-Shui, Hu Xi-Wei. Chinese Physics B 24(9): 095202.

[4] Jeffrey P. Freidberg, Ideal MHD, Cambridge University Press.

[5] Alfvén, Hannes, 1942, Nature, 150 (3805): 405–406.

[6] Gekelman, 1997, Plasmas Physics, Cont. Fusion, 39 A101.

[7] Chen, F.F., Introduction to Plasma Physics and Controlled Fusion, Springer International Publishing.

[8] S. D. Pinches, 1996, Thesis submitted to the University of Nottingham for PhD.

[9] Heyvaerts, J., Priest, E. R., 1983, Astronomy and Astrophysics, 117(2):220-234

[10] W. W. Heidbrink, 2008, Physics of Plasmas, 15 055501

[11] Hartmut Z., Magnetohydrodynamic Stability of Tokamaks, Wiley Publishing

[12] Jeffrey P. Freidberg, Plasma Physics and Fusion Energy, Cambridge University Press.

[13] Y. Todo and T. Sato, 1998, Phys. Plasmas, 5 1321

[14] Y. Todo, 2006, Phys. Plasmas, 13 082503

[15] Y. Todo, H. L. Berk, B. N. Breizman, 2012, Nuclear Fusion, 52 094018

[16] V. M. Nakariakov, B. Roberts, K. Murawski, 1997 , Solar Physics, 175:93-105

[17] Gert J. J. Botha, T. D. Arber, V. M. Nakariakov, F. P. Keenan, 2000, Astronomy and Astrophysics, 363(3)1186-1194